

Rapid Assessment of Power Requirements and Optimization of Thermal Ice Protection Systems

Mayank V. Bendarkar*, Imon Chakraborty[†], Elena Garcia[‡], and Dimitri N. Mavris[§]

Georgia Institute of Technology, Atlanta, GA, 30332

A thermal ice protection system prevents or dispatches ice formed on critical aircraft components like wings or nacelles by heating them either through electro-thermal or pneumatic means. The power requirements for such a system are a function of flight and atmospheric conditions and protected surface area. The developed analysis framework allows evaluation of transient and steady-state cases, anti-icing and de-icing designs, as well as evaporative and running-wet operation. To enable these analyses, a flow solver is first used to calculate local water catch efficiencies and convective heat transfer coefficients on an airfoil. These are then used within a thermal solver which evaluates water and ice accumulations over multiple control volumes under different cases of interest. This control volume approach includes both thermal and mass balances to track temperatures of the protected surface, ice, and water, as well as water/ice layer thicknesses and the water mass flow in or out of the control volume through evaporation or runback. Finally, this tool can yield power requirements for different system layouts and operating conditions, or optimize the protected surface area for a given airfoil under given operating conditions. This can help designers get an estimate of the power draw, and obtain more information on placement of the IPS on novel configurations during the design space exploration phase itself with greater fidelity and minimal computational costs.

I. Introduction

The aerospace industry is moving towards More Electric Aircraft (MEA) subsystems, and there is much greater focus on efficiency of non-propulsive (secondary) power extraction and utilization. This has resulted in alternative electrothermal approaches for ice protection systems (IPS) that use electric power instead of engine bleed air. While handbook methods that provide preliminary design guidelines and power requirement estimates do exist, there is a need to employ physics-based approaches to better estimate these power requirements for various geometries, operating conditions, and flight conditions. A literature review regarding the modeling of ice protection and ice accretion revealed two approaches that are commonly used. The first uses rules-of-thumb and heuristics to estimate heat requirements under different environmental conditions [1]. The other focuses on the ice accretion phenomena itself, but typically assumes an unheated surface on which the ice/water is deposited [2–4].

This work includes development of models that leverage existing ice accretion literature, with modifications to eliminate the requirement for an unheated surface and perfect thermal contact between the heated surface and accreted ice. The ice accretion process is able to capture heated, unheated, and cyclically heated surfaces. This type of model can be used to estimate water/ice accumulation for a given system over a period of time (transient cases). Alternatively, the user can set certain level of desired protection as a goal (e.g., evaporative conditions, running-wet condition without freezing of runback water, etc.) and obtain an estimate of how much heat must be supplied to the protected surface to obtain the desired goal.

The developed framework analyzes the ice accretion/protection problem through information exchange among the following main analysis modules (see Fig. 1):

- 1) Flow Solver: to determine the net collection efficiency and the convective heat transfer coefficients. It comprises two sub-modules:
 - i) Flow Field Analysis (Sec. II)- to compute the flow velocities around the airfoil section and the convective heat transfer coefficients

*Graduate Researcher, Aerospace Systems Design Laboratory (ASDL), School of Aerospace Engg., AIAA Student Member

[†]Research Engineer II, ASDL, School of Aerospace Engg., AIAA Member

[‡]Research Engineer II, ASDL, School of Aerospace Engg., AIAA Member

[§]S.P. Langley Distinguished Regents Professor and ASDL Director, School of Aerospace Engg., AIAA Fellow

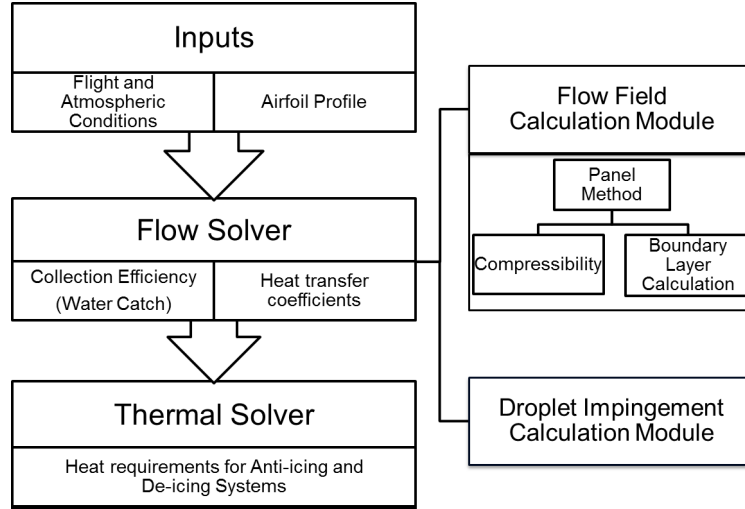


Fig. 1 Main modules of developed approach

- ii) Droplet Impingement Calculation (Sec. III)- to calculate the trajectories of supercooled water droplets to determine whether they impinge on the airfoil surface or miss it (collection efficiency)
- 2) Thermal Solver (Sec.V): to track temperatures and thicknesses of ice and water and determine the heating requirements for a given geometry, flight condition, and operating condition

A. Icing Conditions

There are three basic types of ice accumulation on the aircraft surface: rime ice, glaze ice, and frost. Rime ice forms when water drops are small and freeze rapidly before spreading over the aircraft surface. Glaze ice forms as the water droplets flow over the surface of the aircraft. Frost forms when water freezes on an unprotected aircraft surface when the aircraft is stationary. An important parameter that influences ice formation is the Liquid Water Content (LWC) of air. It includes water in droplet form (not in vapor form) and is expressed in grams per cubic meter. Typical ranges for values are $0.1 - 0.8 \text{ g/m}^3$ for layer type clouds, and $0.2 - 2.5 \text{ g/m}^3$ for cumulus clouds. Water droplet diameter in these clouds is usually $2 - 50$ micron [5].

Stratiform (layer type) and cumuliform (vertical development) are the two general types of clouds pertinent to aircraft icing. Traditionally, continuous maximum (stratiform clouds) conditions have been applied to airframe ice protection and intermittent maximum (cumuliform clouds) conditions have been applied to engine ice protection. The limiting icing envelope in terms of altitude and temperature is specified in FAR §25, Appendix C [6], and in EASA CS-25, Appendix C [7] through the charts shown in Figures 15 and 16 for stratiform (continuous) and cumuliform (intermittent) clouds. The inter-relationship between the ambient air temperature, the mean effective droplet diameter, and the cloud LWC is shown in Figure 17 [6]. These envelopes are useful for selecting values of icing-related cloud variables for the design of ice protection systems for aircraft. Figure 17 indicates the probable maximum value of LWC for a given temperature and representative droplet size in the cloud.

B. Literature Survey of Available Methods

On one end of the spectrum lie handbook methods that are readily available and are published by various sources- two of which are used here [1, 8]. These methods are based on empirical equations as well as some thermodynamic relationships. They also rely on some relatively simple assumptions that include using average values for Reynolds number, water catch, temperature, etc., at each point of the wing. Although handbook methods supply a quick and easy estimation of power requirements for assumed IPS approaches, some of the underlying assumptions and simplifications limit the accuracy of the results, especially if the geometry or flight conditions of interest differ significantly from those that the methods are based upon. Their simplified empirical relationships were instead used as a first order verification

of the predictions for the model that was created.

On the other end of the spectrum, there are dedicated icing analysis tools, such as LEWICE 3.2, which is an ice accretion and protection software developed by the Icing Technology Branch at NASA Glenn Research Center. It has been widely validated against numerous experimental tests [9].

II. Flow Field Analysis

A. Flow Field Analysis Alternatives

A flow solver is used to determine the velocity at any point in the flow field, to permit droplet trajectory calculations for droplet impingement analysis. An investigation of flow solver alternatives was carried out, categorizing the possible methods in terms of their difficulty. A zeroth order approach is to use existing approximations such as SAE AIR 1168/4 [8] to mimic the flow and droplet trajectory analysis. As mentioned previously, the approach is based on simplified representations that are suitable for early design phases and there is an error associated with it (generally within 10% over a small range of droplet Reynolds numbers [8]). This approach is only limited to some airfoils, ambient temperatures, and altitudes. The other alternative is using a first order panel method which is simple and fast; however, this method cannot include the presence of a boundary layer. Hence, a second order panel method with corrections for compressibility and the presence of a boundary layer (necessary for the calculation of the convective heat transfer coefficients) was ultimately selected. Alternatively, using a Navier-Stokes solver for the flow field analysis could be considered. However, since it is computationally more expensive and does not improve the icing calculation significantly [10, 11], it was not used as a flow field solver. It was more convenient to use a simple model such as panel method with modifications in order to increase the level of accuracy.

For droplet trajectory analysis, the methods given by Thomas and Cassoni [12], Özgen and Canibek [2], as well as Meier and Scholz were collected. While Thomas and Özgen's approaches were similar, Meier's water catch calculation is based on the handbook method [8]. Therefore, development focused on the first two to remove the assumptions embedded in the handbook method.

B. Modified PABLO

Potential Flow about Airfoils with Boundary Layer Coupled One-Way (PABLO) [13] is an open-source MATLAB code that provides potential flow solution to low speed flow over airfoils. The one way coupling for boundary layer calculation uses the inviscid potential flow solution to compute boundary layer, but does not consider the effect of the boundary layer on the flow solution. A linear vortex panel method [14] was employed in the study to obtain the pressure distributions and flow field around the airfoil for droplet trajectory calculations. The distribution of a linear vortex over each panel is given by

$$\gamma(x) = \gamma_c + \gamma_l(x - x_1) \quad (1)$$

where γ_c is the constant part of vortex strength distribution that is computed to ensure continuity of vortex strength at the intersection of two panels. Figure 2 shows one such panel with its vortex distribution $\gamma(x)$ and its local coordinate system. The airfoil is discretized into multiple such panels with every panel having its own linear vortex strength distribution, with the condition that the vortex strengths at panel end points be continuous. PABLO was modified to allow the user to define non-unit chord length and free-stream velocity.

C. Flow Field Solution

PABLO only solves for flow characteristics at the surface of the airfoil. In order to obtain flow velocities at any point P in the flow field, perturbation velocities, also called as induced velocities (u, w) due to a vortex panel are computed using [14],

$$u_c = \frac{\gamma_c}{2\pi} \left[\arctan \frac{z}{x - x_2} - \arctan \frac{z}{x - x_1} \right] \quad (2)$$

$$w_c = \frac{\gamma_c}{4\pi} \left[\ln \frac{(x - x_2)^2 + z^2}{(x - x_1)^2 + z^2} \right] \quad (3)$$

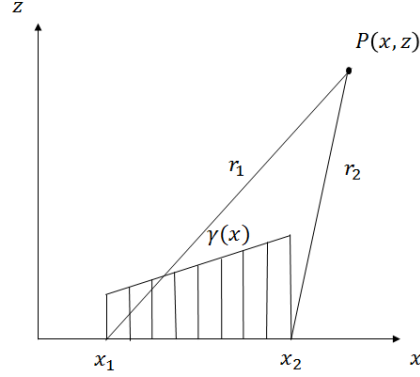


Fig. 2 Velocity induced at a point due to one panel

$$u_l = -\frac{\gamma_l}{4\pi} \left[z \ln \frac{(x-x_1)^2 + z^2}{(x-x_2)^2 + z^2} - 2x \left(\arctan \frac{z}{x-x_2} - \arctan \frac{z}{x-x_1} \right) \right] \quad (4)$$

$$w_l = -\frac{\gamma_l}{2\pi} \left[\frac{x}{2} \ln \frac{(x-x_1)^2 + z^2}{(x-x_2)^2 + z^2} + (x_1 - x_2) + z \left(\arctan \frac{z}{x-x_2} - \arctan \frac{z}{x-x_1} \right) \right] \quad (5)$$

$$u = u_c + u_l \quad (6)$$

$$w = w_c + w_l \quad (7)$$

The arctan functions used in equations 2, 4 and 5 are modified to give values between $-\pi$ to π depending on the location of point P. Equations 6 and 7 give the x, z components of the induced velocity at point P due to one panel in that panel's local coordinates. These contributions by all panels can be superimposed in global coordinates along with the free stream velocity to determine the flow field velocity where desired.

D. Compressibility Correction

It is important to note that Equations 2 to 7 give the flow-field velocities in the incompressible regime. An approximate solution of compressible flow is then obtained by correcting the incompressible C_P values using the Karman-Tsien corrections [15]. The incompressible C_P can be linked to compressible C_{Pc} by the following equations:

$$C_P = 1 - \frac{V^2}{V_{inf}^2} \quad (8)$$

$$C_{Pc} = \frac{C_P}{\sqrt{1 - M_\infty^2} + [M_\infty^2 / (1 + \sqrt{1 - M_\infty^2})] C_P / 2} \quad (9)$$

Assuming isentropic flow, the local Mach number can then be obtained from

$$C_{Pc} = \frac{2}{\gamma M_\infty^2} \left\{ \left(\frac{1 + \frac{\gamma-1}{2} M_\infty^2}{1 + \frac{\gamma-1}{2} M^2} \right)^{\frac{\gamma}{\gamma-1}} - 1 \right\} \quad (10)$$

The flow velocities from this model will be utilized in the droplet trajectory analysis for the calculation of the collection efficiencies and convective heat transfer coefficients as shown in figure 3.

E. Flow Solver Validation

Validation of the flow field solver was performed using experimental data [16] for NACA 0012 airfoil. Figure 4 illustrates the comparison for two different angles of attack. It is seen that the current flow field solver approximates the experimental values of the pressure coefficients with a very good accuracy at different angles of attack.

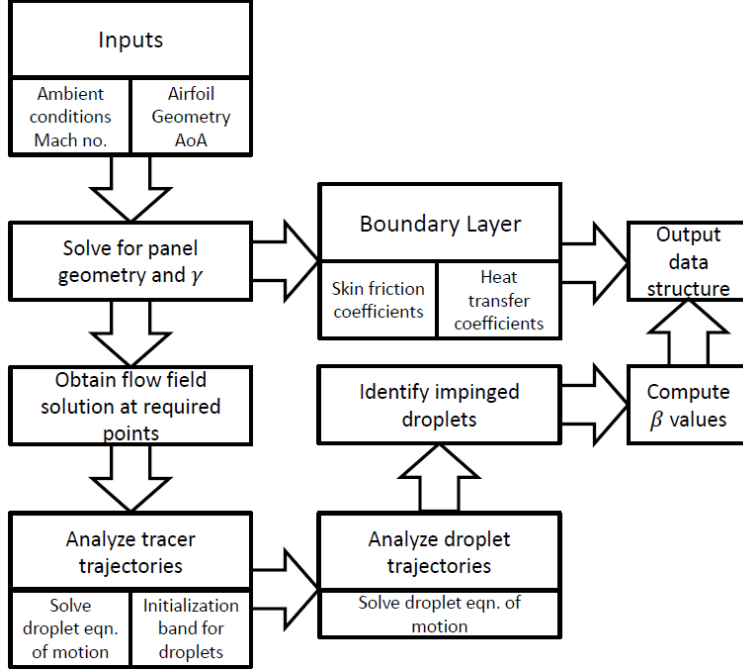


Fig. 3 Flowchart for flowfield and droplet collection efficiency calculations

III. Droplet Trajectory Analysis

A. Droplet Equations of Motion

Droplet analysis was implemented based on the method and equations given by Özgen and Canibek [2]. Droplets are initialized with velocity equal and parallel to the free-stream about ten chord lengths upstream of the leading edge of the airfoil. The liquid water content (LWC) is the weight of liquid water present in a unit volume of air, and is usually expressed in gram per cubic meter. LWC of ambient air and water droplet diameter can be chosen by the user which then determines the separation between two particles. Özgen and Canibek [2]. state the following assumptions as true for droplet diameter $d_p \leq 500\mu m$:

- Droplets remain spherical due to small size
- Droplets do not influence the flow field
- Gravity and aerodynamic drag are the only forces involved

The governing equations for droplet motion are then given as [2]:

$$m\ddot{x}_p = -D\cos\gamma \quad (11)$$

$$m\ddot{z}_p = -D\sin\gamma + mg \quad (12)$$

$$\gamma = \arctan \frac{\dot{z}_p - V_z}{\dot{x}_p - V_x} \quad (13)$$

$$D = 1/2\rho V^2 C_D A_p \quad (14)$$

$$V = \sqrt{(\dot{x}_p - V_x)^2 + (\dot{z}_p - V_z)^2} \quad (15)$$

In equations 11 to 15, m is the droplet mass; $\ddot{x}_p, \ddot{z}_p, \dot{x}_p, \dot{z}_p$ are droplet acceleration and velocity components in x,z direction. A_p is the circular cross section area of every drop, ρ is the local air density computed using isentropic relations and local flow Mach number, and μ is the local viscosity as calculated by the Sutherland viscosity law [17]. C_D is the droplet drag coefficient and is calculated using the following empirical relationship [18]

$$\begin{aligned} C_D &= 1 + 0.197Re^{0.63} + 2.6 \times 10^{-4}Re^{1.38}, \quad Re \leq 3500, \\ C_D &= (1.699 \times 10^{-5})Re^{1.92}, \quad Re \geq 3500 \end{aligned} \quad (16)$$

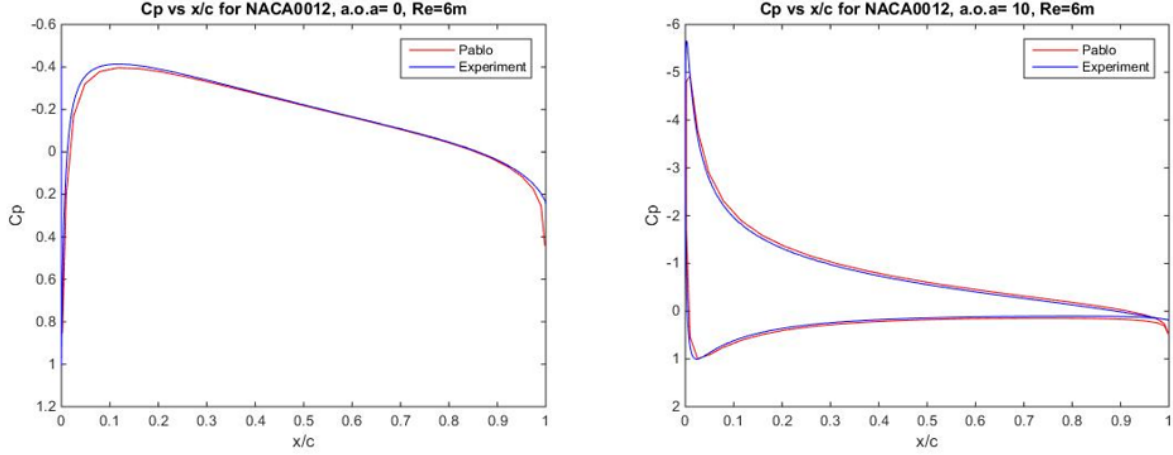


Fig. 4 Flow solver validation versus NACA 0012 experimental data [16] for two different angles of attack

The Reynolds number $Re = \rho V d_p / \mu$ is based on droplet diameter d_p and the relative velocity V . A classical Runge-Kutta integration scheme is used to solve equations 11 to 16 with a sufficiently small time step that ensures accuracy of results. Setting the drag to zero in equation 14 reduces the above equations to those of pure projectile motion under gravity. The solutions were obtained by the classical Runge-Kutta algorithm that is described in Appendix C.

B. Collection Efficiencies

The purpose of the droplet trajectory analysis module is to compute the local water catch and the collection efficiency β , defined as [2]:

$$\beta = \frac{dz_0}{ds} \approx \frac{\Delta z_0}{\Delta s} \quad (17)$$

where dz_0 is the distance between two water droplets at the release plane and ds is the distance between the impact points of same two droplets on the airfoil. Inside the solver, the accelerations and velocities of any impinging particles are artificially set to zero to ensure those droplets hold their position till the end of simulation. Once the simulation ends, these droplets are assumed to impinge on the airfoil panels that have the least distance of their mid points with the droplets. Δs in this case becomes the corresponding panel length, and Δz_0 can be computed based on how many droplets impinge on a particular panel and the droplet spacing during initialization. When the droplet impingement module is initialized with airfoil definition and ambient conditions, a few tracer droplets are fired between $z = -0.5$ to 0.5 m upstream. These tracer droplets identify the band of droplets that will impinge on the airfoil. In the next run, only the droplets in this band are simulated to save simulation time. Droplet separation of 10^{-4} m is assumed to find collection efficiencies and to make it easier to validate them against literature [2].

An example of the results generated by this module is shown in Figs. 5 and 6. Figure 5 shows collection efficiencies calculated for NACA 0012 with a 1m chord at Mach 0.2 plotted against chord normalized arc length with origin located at the leading edge. Figure 6 shows an example case of droplets impinging on a NACA 0012 airfoil at 4 degrees angle of attack. Since the β values are calculated discretely for every panel based on its length and the total number of droplets striking it, some non-smooth transitions between panels might be observed. The location of the peak value, the total collection efficiency, and the skewness of distribution of collection efficiency match what is observed in literature [2].

IV. Calculation of Convective Heat Transfer Coefficients

The convective heat transfer coefficient is a significant factor in the icing process. An Integral Boundary Layer method suggested by Gent et al. [18] is employed here to calculate the heat transfer coefficients for laminar and turbulent boundary layers separately. Heat transfer coefficient for laminar flow is calculated using the formula given by Smith and

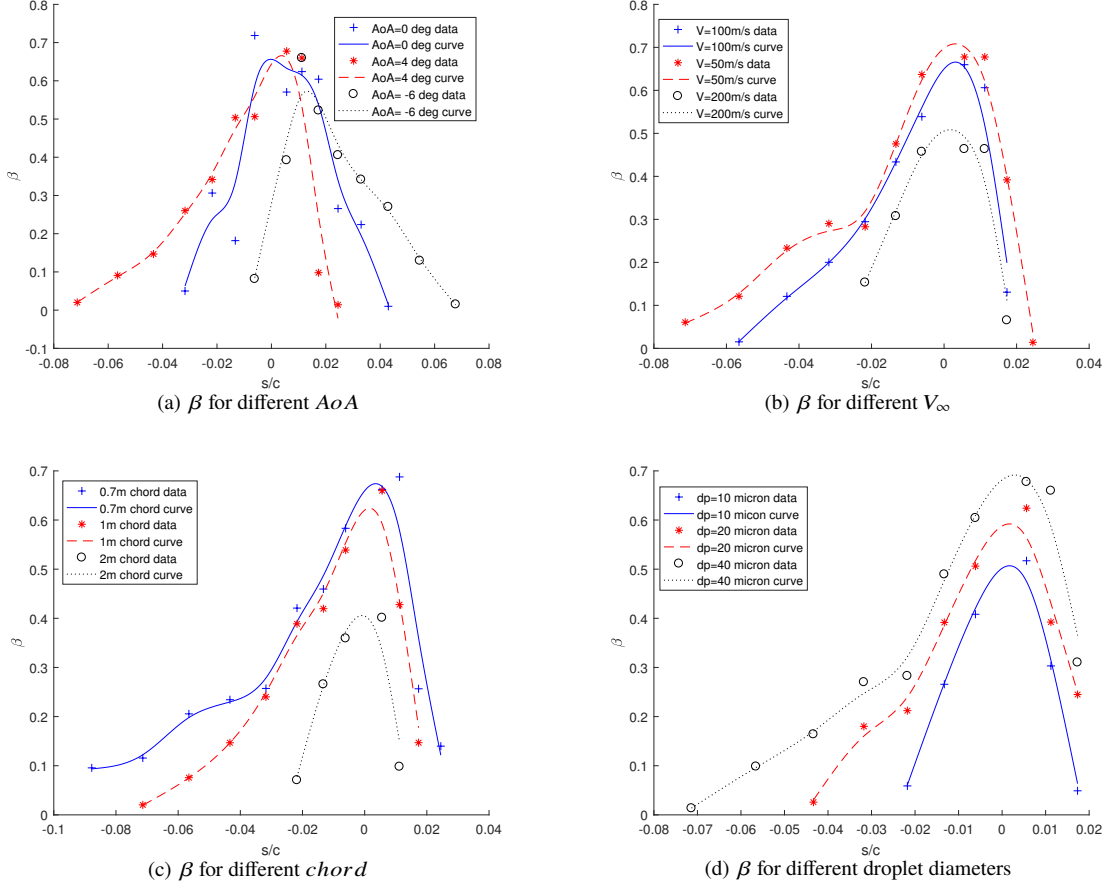


Fig. 5 Results for NACA 0012 with $chord = 1m$, $M = 0.2$. The peak values, shape, and spread of collection efficiencies match what is available in literature [2]

Spalding [19]:

$$h_c = \frac{0.296kU_e^{1.694}}{\sqrt{\nu \int_0^s U_e^{1.87} ds}} \quad (18)$$

where k is the thermal conductivity of air, s is the surface distance from the stagnation point, ν is the kinematic viscosity of air and U_e is the velocity at the edge of the boundary layer. It should be noted that the equation for the laminar heat transfer coefficient is not dependent on roughness unlike that for turbulent flow[18]. For the turbulent flow, the convective heat transfer coefficients are evaluated using the method of Kays and Crawford [20].

$$h_c = St\rho U_e C_p \quad (19)$$

where C_p is the specific heat capacity at constant pressure for air. The Stanton number, St is calculated by [18]:

$$St = \frac{\frac{1}{2}c_f}{Pr_t + \sqrt{\frac{1}{2}c_f/St_k}} \quad (20)$$

where c_f , the skin friction coefficient is obtained from the flow solver. $Pr_t = 0.9$ for the turbulent boundary layer. The roughness Stanton number, St_k is calculated using the equation [18]:

$$St_k = 1.92 Re_k^{-0.45} Pr^{-0.8} \quad (21)$$

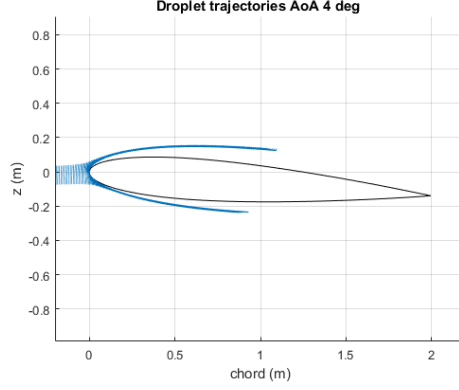


Fig. 6 Droplet trajectories on NACA 0012 at $AoA = 4^\circ$

where $Pr = 0.72$ which is the laminar Prandtl number. The roughness Reynolds number, Re_k is defined as:

$$Re_k = \frac{\rho U_k k_s}{\mu} \quad (22)$$

where U_k is the local velocity at the roughness height and k_s is the roughness height. U_k value is determined by the flow solver at roughness height. The roughness height is calculated by [2]:

$$k_s = \left(\frac{4\sigma_w \mu_w}{\rho_w F \tau} \right)^{\frac{1}{3}} \quad (23)$$

where σ_w , μ_w , ρ_w are the surface tension, viscosity and the density of water respectively. F represents the fraction of the airfoil surface wetted by the water droplets and τ is the local surface shear stress. The local surface shear stress is predicted using the skin friction coefficient.

$$\tau = 0.5 \rho_\infty U^2 c_f \quad (24)$$

where U is the tangential velocity distribution on the airfoil's surface.

The heat transfer coefficients are calculated for the upper and lower surfaces of the airfoil. For the analysis, it is assumed that the flow field velocities at the edge of the boundary layer are the same as those on the airfoil surface in the inviscid case [15].

V. Heat and Mass Transfer Model (Thermal Solver)

The heat and mass transfer model uses the results from the flowfield analysis and the droplet trajectory analysis to analyze the operation of the IPS and the development of ice and/or water on the protected and unprotected surfaces. The following sections describe (i) the formulation of the control volume based analysis approach (Sec. V.A), (ii) the modeling of relevant heat fluxes (see Appendix A), (iii) the solution approach for various cases involving air, water, ice, and substrate (Sec. V.B and Appendix B), (iv) some basic validation of the implemented approach (Sec. V.C), and (v) logic governing transitions between these cases (Sec. V.D).

A. Problem Formulation

Each panel on the airfoil considered as part of the flowfield and droplet trajectory analyses is considered as a control volume in the heat and mass transfer analysis module. The prior analyses feed information regarding the flight condition, the geometry of the control volume, the local water collection (catch) efficiency, and the convection coefficients. The transient and steady-state behavior within the control volumes are evaluated based on governing equations of heat and mass transfer, boundary conditions that depend on the applicable interfaces (between air, water, ice, and substrate), and temperature profile solutions that assume that the ice and water layers are reasonably thin. These are described in the following sections.

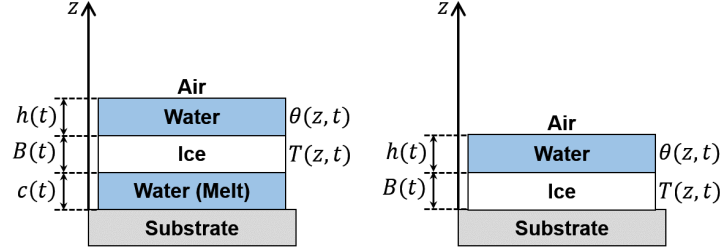


Fig. 7 Control volume setup

1. Governing Equations

The setup of the control volume based mass and thermal flux analysis is based on existing works [3, 4], suitably modified for the current problem. The general setup is shown in Fig. 7, where the temperature of the ice and water layers are denoted by $T(z, t)$ and $\theta(z, t)$ respectively. Their heights are denoted by $B(t)$ and $h(t)$ respectively. If there is, additionally, a layer of water beneath the ice (termed melt), its thickness is represented as $c(t)$. The governing equations for this problem are given by

$$\frac{\partial T}{\partial t} = \frac{k_i}{\rho_i c_i} \frac{\partial^2 T}{\partial z^2} \quad (25)$$

$$\frac{\partial \theta}{\partial t} = \frac{k_w}{\rho_w c_w} \frac{\partial^2 \theta}{\partial z^2} \quad (26)$$

$$\rho_i \frac{\partial B}{\partial t} + \rho_w \frac{\partial h}{\partial t} + \rho_w \frac{\partial c}{\partial t} = m''_{imp} + m''_{in} - m''_{e,s} - m''_{out} \quad (27)$$

$$\rho_i L_F \frac{\partial B}{\partial t} = k_i \frac{\partial T}{\partial z} - k_w \frac{\partial \theta}{\partial z} \quad (28)$$

$$(mC_p)_{sk} \frac{dT_s}{dt} = Q_{ips} - Q_{surf} \quad (29)$$

Equations 25 and 26 are the one-dimensional heat transfer equations through ice and water respectively, with k , ρ , and c denoting thermal conductivity, density, and specific respectively for ice and water (subscripts 'i' and 'w'). Equation 27 represents conservation of mass and relates the change in ice and water thicknesses with the mass fluxes due to water impingement (m''_{imp}), runback water coming in from the upstream control volume (m''_{in}), water evaporation or ice sublimation ($m''_{e,s}$), and runback water flowing into the downstream control volume (m''_{out}). Equation 28 is the Stefan condition at the moving ice/water interface. Equation 29 governs the evolution of the substrate temperature T_s when the thermal mass $(mC_p)_{sk}$ (defined per unit area) associated with the control volume is subjected to the IPS-supplied heat flux Q_{ips} and also the heat flux Q_{surf} at the interface with either air, water, or ice. Evaluating the above system of equations requires (i) modeling heat fluxes corresponding to each of the heat transfer processes occurring and (ii) enforcing the appropriate boundary conditions. These are described in the following sections.

2. Boundary Conditions

For time-domain simulations, the substrate is assumed to be initially clean, i.e., free from ice and water. Thus, at the start of the simulation time interval,

$$B(0) = h(0) = c(0) = 0 \quad (30)$$

At the freezing front or ice/water interface, the ice and water are at the freezing temperature. Thus,

$$T(B, t) = \theta(B, t) = T_f = 273.15 \text{ K} \quad (31)$$

It should be noted that if there is melt beneath the ice ($c > 0$), then that creates an additional ice/water interface, which is also at the freezing temperature T_f . Situations with $c > 0$ may arise during de-icing simulations, and are covered

separately in Sec. VII.13 and Sec. VII.14. The discussion that follows uses the more common case where $c = 0$ to explain the boundary conditions and thin film approximation.

At the free surface (which may be above either ice or water), a cooling condition that features heat fluxes due to convection (Q_c), latent heat release (Q_l), sensible heating (Q_d), heat of entering runback water (Q_{in}), heat of exiting runback water (Q_{out}), evaporation (Q_e) or sublimation (Q_s), aerodynamic heating (Q_a), and kinetic heating (Q_k). The equations for calculating these are included in Appendix A. Thus,

$$-k_w \left. \frac{\partial \theta}{\partial z} \right|_{z=B+h} = (Q_c + Q_d + Q_e + Q_{out}) - (Q_a + Q_k + Q_{in}) \quad (32)$$

$$-k_i \left. \frac{\partial T}{\partial z} \right|_{z=B} = (Q_{ci} + Q_d + Q_s) - (Q_{ai} + Q_k + Q_l) \quad (33)$$

A cooling condition is also applied at the interface between the substrate and the ice or water. Thus,

$$-k_i \left. \frac{\partial T}{\partial z} \right|_{z=0} = H_{is} (T(0, t) - T_s) \quad (34)$$

$$-k_w \left. \frac{\partial \theta}{\partial z} \right|_{z=0} = H_{ws} (\theta(0, t) - T_s) \quad (35)$$

where H_{is} and H_{ws} are respectively the heat transfer coefficients at the ice/substrate or water/substrate interfaces.

3. Temperature Profiles Under Thin Film Approximation

Under the assumption of a thin film for both ice and water, the heat equations may be simplified to quasi-steady forms [3, 4]

$$\frac{\partial^2 T}{\partial z^2} \approx 0, \quad \frac{\partial^2 \theta}{\partial z^2} \approx 0 \quad (36)$$

The reduction of the heat equations from partial differential equations (Eq. 25 and Eq. 26) to ordinary differential equations (Eq. 36) yields what is referred to as a quasi-steady or pseudo-steady problem. The physical interpretation is that the timescales for ice and water growth (which are related to the mass flux of incoming fluid) are much slower than that for heat conduction through ice and water layers [4], giving the temperatures within the layers time to equilibrate. It has been shown [4] that this assumption is valid provided the ice and water thicknesses are considerably less than 2.4 cm and 3 mm respectively, which are within the limits expected in aircraft icing simulations. Integration of Eq. 36 results in temperature solutions for ice and water that are linear in z but not in t , which are of the form

$$T(z) = D_1 z + D_0, \quad \theta(z) = E_1(z - B) + E_0, \quad (37)$$

in which the temperature gradients are constants for given ice and water layer thicknesses, and are given by

$$\frac{\partial T}{\partial z} = D_1, \quad \frac{\partial \theta}{\partial z} = E_1. \quad (38)$$

B. Solution Approach for Specific Cases

As stated previously, the protected surface may be in contact with air, ice, or water. Further, a film of water may rest on top of a layer of ice, and a thin film of water may exist below a layer of ice (if heat is supplied through the protected surface). Thus, the following cases arise (moving from air towards substrate):

- 1) Air-Water-Ice-Substrate (AWIS)
- 2) Air-Substrate (AS)
- 3) Air-Water-Substrate (AWS)
- 4) Air-Ice-Substrate (AIS)
- 5) Air-Water-Ice-Water-Substrate (AWIWS)
- 6) Air-Ice-Water-Substrate (AIWS)

In the solution approaches for each of these cases, the following must be noted:

- The initial temperature solutions do not preclude the possibility of $T(z, t) > T_f$ (ice above freezing temperature or $\theta(z, t) < T_f$ (water below freezing temperature. Thus, the conditions $T(z, t) \not> T_f$ and $\theta(z, t) \not< T_f$ are enforced thereafter.

- The vapor pressure constant e_0 is computed using the air temperature along with the temperature at the air/ice, air/water, or air/substrate interface (as the case may be).
- For air/water and air/ice interfaces, the interface temperature influences the evaporation and sublimation heat fluxes respectively. At the same time, these heat fluxes influence the temperature profile solution that yields the interface temperatures. The interface temperature is, therefore, found through an iterative procedure.

The general method for solving for the different cases involves solving for the temperature profile of ice and water (wherever applicable) using appropriate boundary conditions, and then solving for the growth rates of ice and water using Stefan condition (Eq. 28) and the mass conservation equation (Eq. 27). Detailed solution for the AWIS case is given below as an example, while the pertinent boundary conditions and equations for all other cases are provided in Appendix B.

1. Air-Water-Ice-Substrate (AWIS)

Consider the mass balance equation (Eq. 27), re-arranged to keep exit runback water \dot{m}_{out} and water film height on the LHS:

$$m''_{out} + \rho_w \frac{\partial h}{\partial t} = m''_{imp} + m''_{in} - m''_e - \rho_g \frac{\partial B}{\partial t} \quad (39)$$

Essentially, this states that any mass flux remaining after accounting for the RHS terms, (1) impingement, (2) incoming runback, (3) evaporation, and (4) freezing must result in exit runback water (\dot{m}_{out}) and/or an increase in water film height h . In reality, the shear forces due to the flow of air prevent build-up of the water film beyond a certain height, typically of the order of 0.1 mm [21]. However, in the absence of an air shear model, it is not possible to compute this height explicitly, and then allocate the mass flux residual (RHS) to the two terms on the LHS. Therefore, this work assumes a threshold $h^* = 0.13$ mm based on Myers et al. [21]. With this, the following simplifying assumption is made:

- 1) For $h < h^*$, it is assumed that $m''_{out} = 0$, thus, there is no exiting runback water. The rate of change of water film height is then obtained from Eq. 39.
- 2) For $h \geq h^*$, it is assumed that $\frac{\partial h}{\partial t} \neq 0$, thus, there is no further increase in water film height. Eq. 39 is used to compute the mass flux of exiting runback water.

The temperature distribution in the ice layer of thickness B is subject to the boundary conditions

$$T(z = B) = T_f, \quad k_i \frac{\partial T}{\partial z} \Big|_{z=0} = H_{is}(T(0, t) - T_s), \quad (40)$$

applying which, the temperature solution is given by

$$T(z) = D_1 z + D_0, \quad D_0 = \frac{k_i T_f + H_{is} T_s B}{k_i + H_{is} B}, \quad D_1 = \frac{H_{is}(T_f - T_s)}{k_i + H_{is} B}. \quad (41)$$

The temperature distribution in the water layer of thickness h is subject to the boundary conditions

$$\theta(z = B) = T_f, \quad k_w \frac{\partial \theta}{\partial z} \Big|_{z=B+h} = Q_a + Q_k - Q_c - Q_d - Q_e, \quad (42)$$

applying which, the temperature solution is given by

$$\begin{aligned} \theta(z) &= E_1(z - B) + E_0, \quad E_0 = T_f, \quad E_1 = \frac{a_0 - a_1(T_f - T_a)}{1 + a_1 h}, \\ a_0 &= \frac{r H_{aw} V_\infty^2}{2 c_a k_w} + \frac{\beta V_\infty^3 G}{2 k_w}, \quad a_1 = \frac{H_{aw} + \beta V_\infty G c_w + \chi e_0}{k_w} \end{aligned} \quad (43)$$

For Case 1, $h < h^*$, the exiting runback water mass flux is set to zero: $m''_{out} = 0$. The rate of change of ice thickness is given by introducing the temperature gradients $\frac{\partial T}{\partial z}$ and $\frac{\partial \theta}{\partial z}$ into the Stefan condition and solving for the ice growth rate $\frac{\partial B}{\partial t}$:

$$\begin{aligned} \frac{\partial B}{\partial t} &= \frac{a_2}{a_4 + B} - \frac{a_3}{1 + a_1 h} - \frac{m''_{in} c_w \tilde{\theta}_{rb, in}}{\rho_g L_F}, \\ a_2 &= \frac{k_i(T_f - T_s)}{\rho_g L_F}, \quad a_3 = \frac{k_w \{a_0 - a_1(T_f - T_a)\}}{\rho_g L_F}, \quad a_4 = \frac{k_i}{H_{is}} \end{aligned} \quad (44)$$

The rate of change of water film height is then found using the continuity equation (Eq. 39) with exiting runback water mass flux m''_{out} set to zero:

$$\frac{\partial h}{\partial t} = \frac{m''_{imp} + m''_{in} - m''_e - \rho_g \frac{\partial B}{\partial t}}{\rho_w} \quad (45)$$

For Case 2, $h \geq h^*$, the water film growth rate is initially set to zero: $\frac{\partial h}{\partial t} = 0$. The rate of change of ice thickness is given by

$$\frac{\partial B}{\partial t} = \frac{1}{1 + c_w \tilde{\theta}_{rb,out} / L_F} \left\{ \frac{a_2}{a_4 + B} - \frac{a_3}{1 + a_1 h} - \frac{m''_{in} c_w \tilde{\theta}_{rb,in}}{\rho_g L_F} + \frac{(m''_{imp} + m''_{in} - m''_e) c_w \tilde{\theta}_{rb,out}}{\rho_g L_F} \right\}. \quad (46)$$

Next, the mass flux of exiting runback water is computed based on mass conservation as

$$m''_{out} = m''_{imp} + m''_{in} - m''_e - \rho_g \frac{\partial B}{\partial t}. \quad (47)$$

However, if the above yields $m''_{out} < 0$, then it is assumed that there is no exiting runback water, and that the water film height is instead decreasing. Thus, with a setting of $m''_{out} = 0$, the rate of change of ice thickness is computed using Eq. 44, and the rate of change of water film height is computed using Eq. 45 (equivalent to Case 1).

C. Validation of AIS and AWIS Scripts

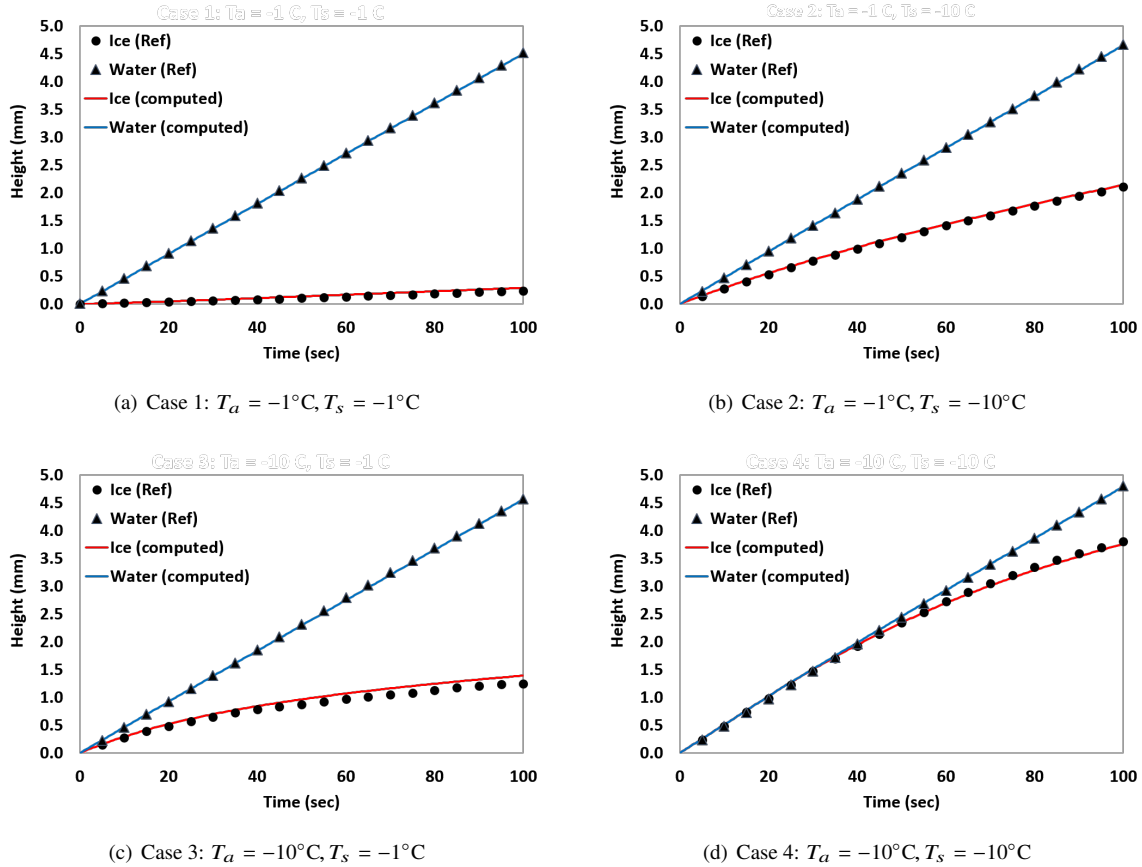


Fig. 8 Validation against Myers & Hammond [3]

To verify the implementation of the method, results for a single control volume were validated against the results presented by Myers and Hammond [3], as shown in Fig. 8. For this purpose, the upper bound on water film thickness

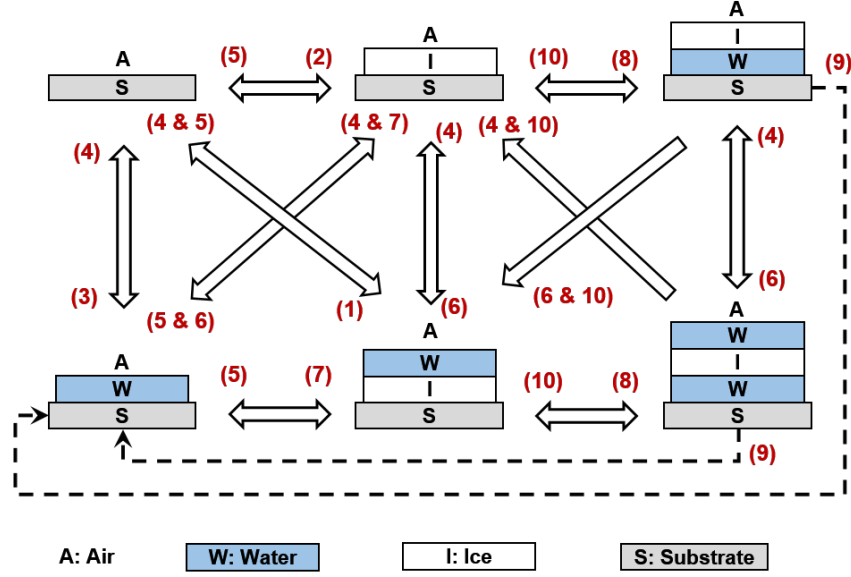


Fig. 9 Transitions considered between AS, AWIS, AWS, AIS, AWIWS, and AIWS conditions. The numbers in parentheses near arrow-heads (see Table 1) refer to the test condition to determine whether a transition is required

($h^* \approx 0.1$ mm) was relaxed and all model parameters were matched up. Cases 1-4 feature different combinations of ambient temperature T_a and substrate surface temperature T_s . For cases 1-3, ice and water grow simultaneously throughout the simulation. For case 4, water appears after about 25 seconds, prior to which there is accumulation of rime ice. The ice growth increases for both lower air and substrate temperatures, but the latter has the more pronounced effect.

D. Transitions Between AS, AWIS, AWS, AIS, AWIWS, and AIWS Conditions

During the course of a time-domain simulation, the condition existing on the substrate may change. As evident from the preceding sections, this implies a change in the corresponding boundary conditions existing at the relevant interfaces, and thus a need to transition between analysis scripts as required. The transition logic that governs the transitions between AS, AWIS, AWS, AIS, AWIWS, and AIWS conditions is summarized in Fig. 9 and Table 1. Transitions may be initiated based on

- 1) Calculated positive or negative values of ice and water growth rates ($\frac{\partial B}{\partial t}$, $\frac{\partial h}{\partial t}$),
- 2) Impending disappearance of ice, water, or melt layers based on corresponding thicknesses and rates (B and $\frac{\partial B}{\partial t}$, h and $\frac{\partial h}{\partial t}$, c and $\frac{\partial c}{\partial t}$),
- 3) Calculated above-freezing temperatures ($T(z) > T_f$) within ice layer,
- 4) Melt thickness in excess of selected threshold ($c \geq c^*$) leading to shedding of ice layer.

Under the assumption that the substrate is initially clean, the simulation is started by setting the Air-Substrate (AS) as the active condition. Thereafter, the transition logic (Fig. 9 and Table 1) governs the switching between the different conditions as the simulation progresses.

VI. Integrated Model Results

Traditional IPS sizing approaches look at a point solution to determine requirements [1], and cannot be generalized for evaluating unique cases that may interest an aircraft designer. In the proposed approach, flow-field analysis (Sec. II), droplet trajectory analysis (Sec. III), and the thermal solver (Sec. V) were integrated to develop a model that is flexible enough to allow a time domain simulation where heat flux is provided as a function of time (and location of protected panel) to determine the growth of ice and water on an airfoil under different icing conditions. This capability can also be

Table 1 Transition logic between AS, AWIS, AWS, AIS, AWIWS, and AIWS conditions (see also Fig. 9). To read: (1) select “From” and “To” cases in transition matrix, (2) Locate Note # corresponding to selected row and column, (3) Read off test condition corresponding to Note # from lower table.

From ↓	← To →					
	AS	AWIS	AIS	AWS	AWIWS	AIWS
AS	0	1	2	3		
AWIS	4 & 5	def.	4	5	8	
AIS	5	6	def.	5 & 6		8
AWS	4	7	4 & 7	def.		
AWIWS		10	4 & 10	9	def.	4
AIWS		6 & 10	10	9	6	def.
Note #	Condition(s) necessary for transition					
0	$\left(\frac{\partial B}{\partial t}\right)_0 < 0, \left(\frac{\partial h}{\partial t}\right)_0 < 0$, Eq. 68					
1	$\left(\frac{\partial B}{\partial t}\right)_0 > 0, \left(\frac{\partial h}{\partial t}\right)_0 > 0$, Eq. 68					
2	$\left(\frac{\partial B}{\partial t}\right)_0 > 0, \left(\frac{\partial h}{\partial t}\right)_0 < 0$, Eq. 68					
3	$\left(\frac{\partial B}{\partial t}\right)_0 < 0, \left(\frac{\partial h}{\partial t}\right)_0 > 0$, Eq. 68					
4	$h + \left(\frac{\partial h}{\partial t}\right) \Delta t < 0$					
5	$B + \left(\frac{\partial B}{\partial t}\right) \Delta t < 0$					
6	$\frac{\partial h}{\partial t} > 0$					
7	$\frac{\partial B}{\partial t} > 0$					
8	$T(z = 0) > T_f$					
9	$\frac{\partial c}{\partial t} > 0, c > c^*$ (ice shedding)					
10	$c + \left(\frac{\partial c}{\partial t}\right) \Delta t < 0$					
def.	default (if no other condition is satisfied)					

used to optimize the heat flux required to establish evaporative or running-wet conditions. The method used to calculate the power requirements for evaporative and running-wet de-icing is explained in the following sub-sections. In all the following results, values for h_{ai} , h_{as} , and h_{aw} are assumed to be the same and are obtained using Eq. 18, 19, while h_{is} and h_{ws} are assumed as 1000 W/K/m^2 .

A. Time-Domain Simulation of De-Icing Process

For a generic (unspecified) airfoil, Krammer and Scholz [1] calculated a power requirement of 16.35 kW/m^2 assuming 70% efficiency for electric heaters and a heat-on time of 9 seconds in a total cycle of 3 minutes using a handbook method[8]*. In the developed model, a Boeing 737 midspan airfoil was simulated under typical icing conditions mentioned in Fig.10. A heat-flux of 14.29 kW/m^2 was found to be sufficient to de-ice the airfoil at the end of the heat-on cycle assuming 70% efficiency.

Figure 10 shows the global variation of water and ice layer thicknesses over time and also over the surface of the airfoil. Heat flux is provided for 9 seconds after letting ice accumulate for 171 seconds. The reduction in ice thickness to zero can be seen in Fig.10. Two such cycles are shown. While the water layer thickness is capped at 0.13 mm as mentioned before, growth in water thickness on the downstream surfaces can also be seen as time progresses. The deicing cycle is clearer from Fig. 11, which focuses on the first lower surface control volume from the leading edge. It is interesting to note that for the second heating cycle, lesser amount of ice accumulates over the same time period. At the

*Krammer and Scholz note that this value obtained after their replication of a handbook method is still lower than a suggested value of 34.1 kW/m^2 by the same handbook. However, they note that numerous assumptions like effective water catch, heat-on time etc. can have a large impact on power required. For e.g. if heat-on time is reduced to 2.5 sec instead of 9 sec, suggested heating power required increases to 62 kW/m^2

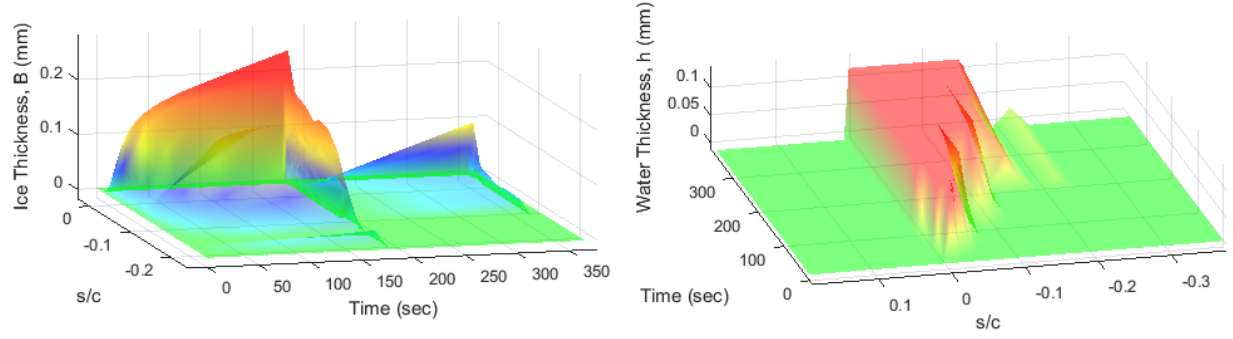


Fig. 10 Ice and water layer thickness variation on B737 airfoil during de-icing simulation (*Flight condition : $0ft$, $dISA = -18K$, $M = 0.265$, $AoA = 8^\circ$, $LWC = 0.3g/m^3$, $d_p = 20 \text{ micron}$, $EOP : s/c \in [-0.25, 0.05]$. Unconventional axes orientations are to improve readability of the plots*)

same time, it can be seen that the surface temperature rises quickly due to some of the passive heat fluxes provided in Appendix A, as well as the fact that skin thermal inertia is assumed to be very low with only a 6mm thickness metal skin considered as the substrate.

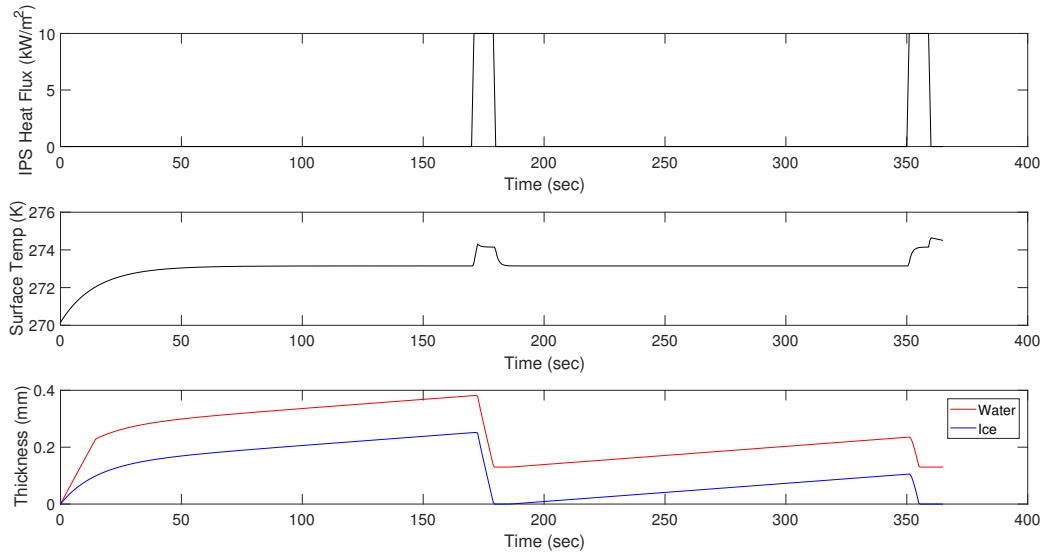


Fig. 11 Variation of IPS heat flux, surface temperature, and ice and water thicknesses for lower surface leading edge control volume during de-icing simulation (*Flight condition : $0ft$, $dISA = -18K$, $M = 0.265$, $AoA = 8^\circ$, $LWC = 0.3g/m^3$, $d_p = 20 \text{ micron}$*)

B. Evaluating Required Heat Flux for Evaporative Anti-Icing

The underlying assumption is that no significant impingement occurs outside of the protected area. The goal of the ‘evaporative’ evaluation mode is to ensure that no runback water exits the protected area. In other words, while water (but not ice) may exist on the surface of the protected area, it must be evaporated off prior to exiting the most downstream control volumes that are supplied with heat by the IPS.

The IPS heat flux Q_{ips} is itself obtained from a gradient-based optimizer (implemented using MATLAB *fmincon* algorithm) in the outer loop by solving the following constrained optimization problem:

- Minimize IPS heat flux Q_{ips} , subject to the following constraints -

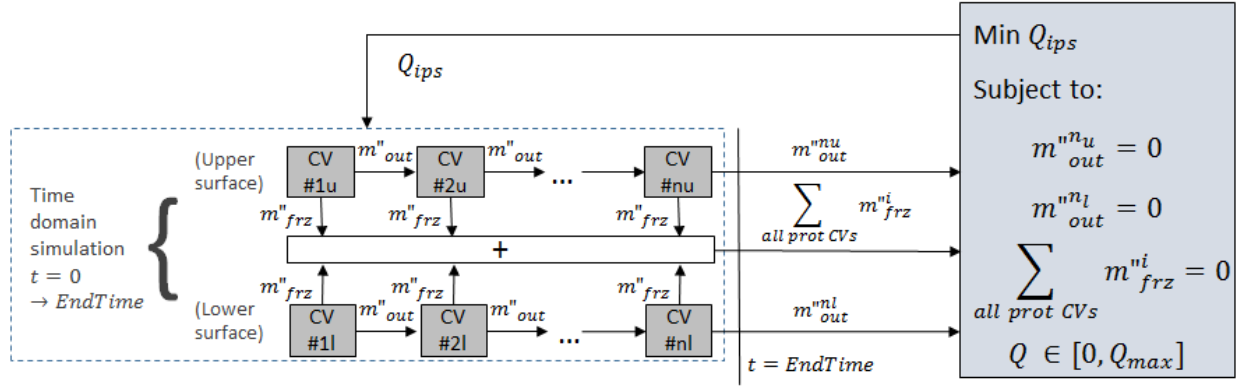


Fig. 12 Optimization outer loop - A gradient-based optimizer (MATLAB *fmincon*) is used to determine the minimum IPS heat flux Q_{ips} required for evaporative conditions (no ice anywhere and no runback water exiting from the protected area)

- 1) $m_{out}^{(nu)} = 0$: no runback water exiting protected area on upper surface
- 2) $m_{out}^{(nl)} = 0$: no runback water exiting protected area on lower surface
- 3) $\sum_i m_{frz}^{(i)} = 0$: no freezing occurring in any protected control volume
- 4) $Q_{ips} \in [0, Q_{ips}^{max}]$: side constraints (bounds) for IPS heat flux

Solution of the above optimization problem at a given flight condition yields the minimum IPS heat flux required to achieve evaporative conditions at that flight condition. Figure 12 shows the implementation of the optimization approach. The time-domain simulation capability is leveraged to find the optimum heat flux needed to attain evaporative conditions within a user defined time limit (EndTime). Since the steady state solution can be considered to correspond to an end-time of ∞ , this approach gives power requirements that are slightly higher than true steady state values, and is hence conservative.

1. Constant Q_{ips} to Protected Area

One approach towards anti-icing is to supply a constant heat flux to the entire ice protected area, which also corresponds to how most pneumatic IPS work. For a B737 airfoil, a constant heat flux of 14.29 kW/m^2 with 70% efficiency was found to be sufficient to achieve evaporative conditions within 9 seconds (0 ft , $T_\infty = 270\text{K}$, $AoA = 8^\circ$, $LWC = 0.3\text{g/m}^3$, $d_p = 20\text{micron}$, $EOP : s/c \in [-0.25, 0.05]$). While the subsequent power required to maintain evaporative conditions might be lower, this number captures the time-critical nature of attaining evaporative conditions on the wing, and hence gives a conservative estimate.

2. Chord-wise Optimized Q_{ips} to Protected Area

An electric IPS can allow the heat flux to be distributed uniquely to different protected panels depending on their chordwise location. This chord-wise distribution of heat flux can then be optimized for different flight conditions to minimize the total power consumption by the IPS. In this scenario, the objective function in Fig. 12 is replaced by the following:

$$\text{New Objective Function : } \text{Min } \sum Q_{ips}(i) \cdot l(i)$$

Where $Q_{ips}(i)$ is the heat flux supplied to and $l(i)$ is the length of the i^{th} CV. The new objective function essentially tries to minimize the total power needed across all CVs to attain the evaporative case. Figure 13 shows the solution approach described above exercised over the mentioned flight conditions and for three different endtime settings of 9s, 30s, and 60s. It can be seen that as the allowable time to attain evaporative conditions is increased, peak values of Q_{ips} required go down. At the same time, it is interesting to note that the chord-wise distribution of Q_{ips} does not change a lot between endtimes of 30 and 60 seconds. Whether result can be generalized to obtain the true steady state power requirement is a question that cannot be answered without further examination. The chord-wise optimized Q_{ips} distribution over multiple flight conditions can be used to determine the optimum placement of heating surfaces on an

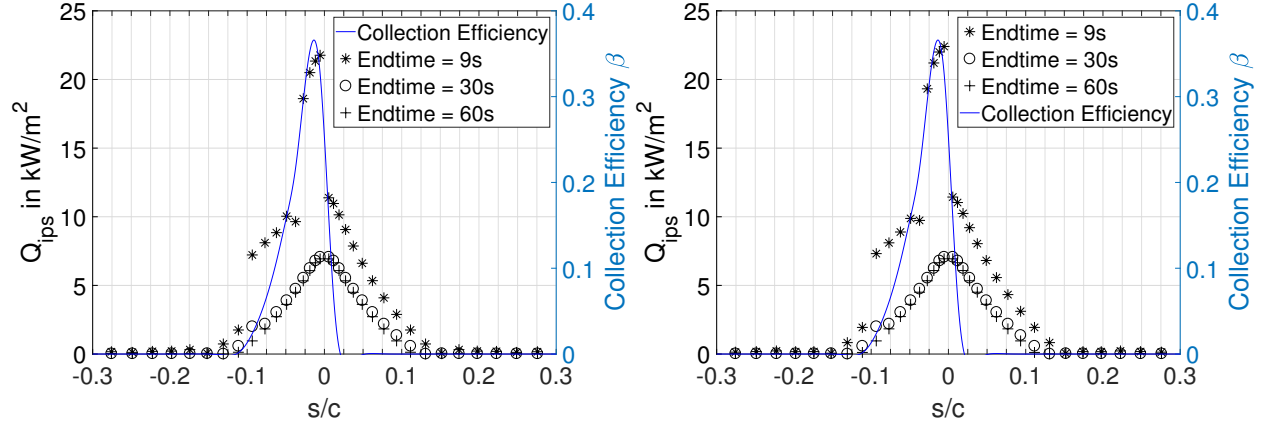


Fig. 13 Chordwise distribution of required heat flux Q_{ips} in kW/m^2 to attain Evaporative (left) and Running-Wet (right) conditions within the time limit specified. (NACA 0012, Flight condition : 0 ft , $dISA = -18\text{K}$, $M = 0.265$, $AoA = 8^\circ$, $LWC = 0.3\text{g/m}^3$, $d_p = 20 \text{ micron}$, $EOP : s/c \in [-0.3, 0.3]$)

airfoil for a electro-thermal IPS. Finally, it is also interesting to note that the distribution of heat flux shows a similar trend to the water catch over the airfoil.

C. Evaluating Required Heat Flux for Running-Wet Anti-Icing

Running-wet conditions can be defined as when water is allowed to exit the thermally protected area, but is not allowed to freeze anywhere on the airfoil. The optimization outer loop in this case is similar to that shown in Fig. 12, except with the requirement of zero runback water relaxed. The requirement that the mass flux due to freezing be zero is still applicable.

1. Constant Q_{ips} to Protected Area

For a B737 airfoil, a constant heat flux of 14.2 kW/m^2 with 70% efficiency was found to be sufficient to achieve running conditions within 9 seconds (0 ft , $T_\infty = 270\text{K}$, $AoA = 8^\circ$, $LWC = 0.3\text{g/m}^3$, $d_p = 20\text{micron}$, $EOP : s/c \in [-0.25, 0.05]$). This number is quite similar to what was obtained for the evaporative case. One potential reason can be that the extent of ice protection is already wide enough to not allow any runback water from exiting the last protected control volume while ensuring ice does not form on the CV with the highest water impingement.

2. Chord-wise Optimized Q_{ips} to Protected Area

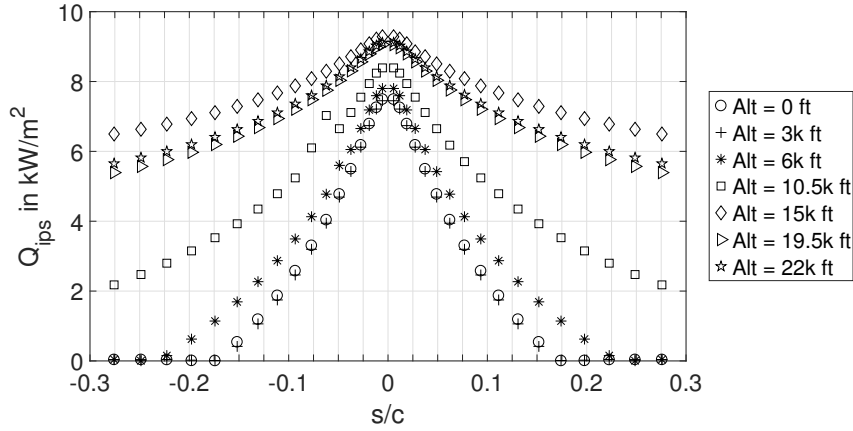
Figure 13 shows the chordwise heat flux required to attain running-wet conditions within 9, 30, and 60 seconds. It is interesting to note that the values for this case are very similar to the evaporative anti-icing case. One potential reason for this can be the way runback water is calculated. The current approach assumes that water does not flow back into downstream control volume unless it reaches the critical height (h^*) of 0.13mm, since an air-shear approach has not been implemented yet. As a result, the runback water constraint is never active given the wide range of the extent of protection. A detailed investigation of this phenomenon will be conducted in the near future.

D. Additional Results

Krammer and Scholz[1] calculated a design power requirement of $14 - 22 \text{ kW/m}^2$ for a continuously heated power strip near the leading edge of a wing. There are multiple issues that a designer may face when using their values. First, the value calculated is assumed to be the peak load of the IPS over the entire mission segment. Second, the assumptions that go into calculating those values are rarely realized by any given aircraft in operation. Third, an aircraft designer might want to know how IPS power requirement varies in a variety of flight conditions so that s/he may manage tradeoffs between secondary power offtakes. For this reason, this tool provides the flexibility to aircraft designers to estimate with greater accuracy, the power requirements under various scenarios.

Table 2 Mission segment details for extreme icing conditions for a commercial aircraft

Segment	Altitude (ft)	Mach no.	AoA ⁰	LWC (g/m^3)	T_∞ (K)
Take Off	0	0.265	8	0.6	263
Climb	3000	0.4	4	0.48	260
Climb	6000	0.42	4	0.36	255
Climb	10500	0.46	4	0.25	248
Climb	15000	0.553	2	0.2	243
Climb	19500	0.597	2	0.2	243
Climb	22000	0.63	2	0.2	243

**Fig. 14 Chordwise distribution of required heat flux Q_{ips} in kW/m^2 to attain evaporative conditions within 60 seconds for flight conditions specified in Table 2 ($d_p = 15$ micron) assuming 100% efficiency**

As an example, IPS power requirements are calculated in the evaporative mode for typical mission segments of a commercial aircraft as detailed in Table 2. While the given altitude, Mach no., and angle of attack (AoA) combinations are typical for a commercial aircraft, the liquid water content and ambient temperature are determined based on the charts given in Appendix D. Figure 14 shows the results obtained for IPS power that is distributed chordwise. It is important to note that the droplet collection efficiency has a different distribution for the different mission segments noted in Table 2, and therefore differences in the predicted extent of protection required (s/c values with non-zero heat required) are expected between different segments. Chakraborty and Mavris [22] have demonstrated in detail how the electrification of IPS can be handled at the conceptual design stage by including considerations like bleed air requirements, ducting and piping changes, weight changes, secondary power off-takes among others. While studying three different aircraft classes for impacts of subsystem electrification, bleedless architectures including electro-thermal IPS were found to dominate the top architectures in all three classes [22]. However, this study was conducted assuming a constant IPS power load determined using the method given by Krammer and Scholz [1]. The methodology developed here can help update this study with more accurate results and improve confidence in the trade-offs that can be expected while transitioning from a pneumatic to electro-thermal IPS.

VII. Conclusions and Future Work

A model to evaluate the power requirement of an optimized thermal ice protection system was developed analytically and implemented in MATLAB. The model validates well against cases available in literature and can be used to simulate ice accretion over an airfoil given a thermal power input or to determine the power required to achieve de-icing or running-wet/evaporative anti-icing capability. It can also be used to evaluate mission specific power requirements, and chord-wise optimized heat flux needed to attain the desired IPS capability. As can be seen, the current results indicate

that more accurate estimates of IPS power requirements can be obtained for different mission segments uniquely, and can potentially help in obtaining more accurate system level impacts of electro-thermal ice protection systems when combined with earlier studies by Chakraborty and Mavris. Additionally, the capability also allows electro-thermal IPS to surgically provide as much heat as is required at a particular chord-wise location and minimize wastage that would occur in pneumatic IPS that would heat the entire protected area equally. The current capability can give aircraft designers greater freedom to pursue novel architectures and wing-geometries knowing that reliable IPS power requirements can be generated as required. Overall, the described method allows designers to burn down some of the epistemic uncertainty in determining IPS power requirements.

In the future, the developed capability will be validated against NASA's LEWICE. Development of an air-shear model to more accurately determine the flow of runback water on the airfoil surface can also be explored. A complete integration of this capability into aircraft conceptual design through an in-house more-electric subsystems architecting tool will be considered to get a more accurate picture of the impact of electro-thermal IPS in more-electric and next-gen aircraft.

Appendix

Appendix A: Modeling of Heat Fluxes

1. Convective Heat Transfer

Convective heat transfer between the water surface at temperature θ_{surf} and the air at temperature T_a is given by [2]

$$Q_c = H_{aw}(\theta_{surf} - T_a), \quad (48)$$

where H_{aw} is the convection coefficient between air and water at the given flight condition. If the surface of ice, at temperature T_{surf} is exposed to air, the convective heat flux is given by

$$Q_{ci} = H_{ai}(T_{surf} - T_a), \quad (49)$$

where H_{ai} is the convection coefficient between air and ice at the given flight condition. If the substrate, at temperature T_s , is exposed to air, the convective heat flux is given by

$$Q_{cs} = H_{as}(T_s - T_a), \quad (50)$$

where H_{as} is the convection coefficient between air and the substrate at the given flight condition.

2. Heat Loss Through Evaporation

The heat flux due to evaporation occurring from the surface of water is given by [2]

$$Q_e = \chi \{e(\theta_{surf}) - e(T_a)\}. \quad (51)$$

The evaporation coefficient χ in Eq. 51 is computed as [4]

$$\chi = \frac{0.622 H_{as} L_E}{c_a p_0 l_e^{2/3}}, \quad (52)$$

where H_{as} is the convection coefficient between air and substrate, L_E is the latent heat of vaporization, c_a is the specific heat of air, p_0 is the ambient pressure, and l_e is the Lewis number.

The quantities $e(T)$ in Eq. 51 denote the saturation vapor pressure at temperature T . For convenience, the term in brackets is expressed as

$$\{e(\theta_{surf}) - e(T_a)\} = e_0(\theta_{surf} - T_a) \implies e_0 = \frac{e(\theta_{surf}) - e(T_a)}{\theta_{surf} - T_a} \quad (53)$$

The vapor pressure constant e_0 is computed from the above using a sixth order polynomial relation for vapor pressure $e(T) = \sum_{i=0}^6 C_i T^i$, with $c_0 = 6984.505294$, $c_1 = -188.9039310$, $c_2 = 2.133357675$, $c_3 = -1.288580973e^{-2}$; $c_4 =$

$4.393587233e^{-5}$; $c_5 = -8.023923082e^{-8}$; $c_6 = 6.136820929e^{-11}$. With the value of e_0 computed, the evaporative heat flux may now be equivalently expressed as

$$Q_e = \chi e_0 (\theta_{surf} - T_a). \quad (54)$$

The corresponding mass flux due to evaporation is given by

$$m_e'' = \frac{Q_e}{L_v} = \frac{\chi e_0 (\theta_{surf} - T_a)}{L_v} \quad (55)$$

3. Heat Loss Through Sublimation

The heat loss due to sublimation of ice is given by [2]

$$Q_s = \chi_s e_0 (T_{surf} - T_a), \quad (56)$$

where the sublimation coefficient χ_s is computed as [4]

$$\chi_s = \frac{0.622 H_{as} L_s}{c_a p_0 l_e^{2/3}}, \quad (57)$$

where L_s is the latent heat of sublimation. The mass flux due to sublimation is given by

$$m_s'' = \frac{Q_s}{L_s} = \frac{\chi_s e_0 (T_{surf} - T_a)}{L_s} \quad (58)$$

4. Cooling due to Incoming Droplets

The heat flux due to cooling by droplets impinging with mass flux $m_{imp}'' = \beta V_\infty G$ is given by [2]

$$Q_d = (\beta V_\infty G) c_w (\theta_{surf} - T_d), \quad (59)$$

where c_w is the specific heat of water. The above is for the case of droplets impinging on to the water film. In case droplets impinge on the surface of ice, θ_{surf} in the above is to be replaced with ice surface temperature T_{surf} . Water droplet temperature T_d is assumed to be equal to the air temperature, $T_d = T_a$.

5. Kinetic Energy of Incoming Droplets

This is computed from freestream velocity V_∞ and impingement mass flux $m_{imp}'' = \beta V_\infty G$ as [2]

$$Q_k = m_{imp}'' \frac{V_\infty^2}{2} = (\beta V_\infty G) \frac{V_\infty^2}{2} \quad (60)$$

6. Aerodynamic Heating

If the free surface is water, then the aerodynamic heating flux is given by [2]

$$Q_a = \frac{r H_{aw} V_\infty^2}{2 c_a}, \quad (61)$$

where c_a is the specific heat of water. The temperature recovery factor r in the above is computed as

$$r = 1 - 0.99 (1 - Pr^n), \quad (62)$$

where Pr is the Prandtl number and the exponent is set to $n = \frac{1}{2}$ for a laminar boundary layer and $n = \frac{1}{3}$ for a turbulent boundary layer.

7. Latent Heat of Solidification

Latent heat release due to the formation of ice is given by [2]

$$Q_\ell = \rho_i L_F \frac{\partial B}{\partial t} \quad (63)$$

8. Heat Flux due to Runback Water Flow

Runback water entering with mass flux m''_{in} and mean temperature $\tilde{\theta}_{rb,in}$ adds energy to the control volume, while runback water exiting with mass flux m''_{out} and mean temperature $\tilde{\theta}_{rb,out}$ removes energy from the control volume. The corresponding heat fluxes are given by [2]

$$Q_{in} = m''_{in} c_w \tilde{\theta}_{rb,in}, \quad Q_{out} = m''_{out} c_w \tilde{\theta}_{rb,out} \quad (64)$$

9. Heat flux at Substrate Surface

If there is a ice/substrate interface (AIS, AWIS), then this is given by $Q_{surf} = H_{is}(T_s - T_0)$, where T_s is the substrate temperature and T_0 is the temperature at the bottom of the ice layer ($z = 0$). Similarly, if there is a water/substrate interface (AWS), then the heat flux at the surface is $Q_{surf} = H_{ws}(T_s - \theta_0)$. If the substrate is in contact with melt (AWIWS, AIWS), whose temperature is assumed to be T_f throughout the film, then the heat flux is given by $Q_{surf} = H_{ws}(T_s - T_f)$. If the substrate is in direct contact with air (AS), the surface heat flux is given by $Q_{surf} = Q_c + Q_e + Q_d - Q_k - Q_a$.

Appendix B: Solution Approach for Other Cases

10. Air-Substrate (AS)

Boundary conditions: $h = 0, B = 0 \implies \partial B / \partial t \not\prec 0, \partial h / \partial t \not\prec 0$

Since $h = 0 < h^*$, there is no exiting runback water, $m''_{out} = 0$. From the mass balance equation, Eq. 27, it is clear that $m''_e \not\prec m''_{imp} + m''_{in}$, thus yielding:

$$m''_e = \min \left(\frac{\chi e_0(T_s, T_a)(T_s - T_a)}{L_F}, m''_{imp} + m''_{in} \right) \quad (65)$$

The net heat flux at the dry surface is then given by

$$Q_{surf} = \left\{ H_{as} + m''_{imp} c_w \right\} (T_s - T_a) + m''_e L_e - \left(m''_{imp} \frac{V_\infty^2}{2} + r H_{as} \frac{V_\infty^2}{2 c_a} \right). \quad (66)$$

Evaporative conditions will continue to persist if $m''_e = m''_{imp} + m''_{in}$. Which imply

$$\frac{\partial B}{\partial t} = 0, \quad \frac{\partial h}{\partial t} = 0 \quad (67)$$

On the other hand, if $m''_e < m''_{imp} + m''_{in}$, then it is possible to have $\frac{\partial B}{\partial t} > 0$ and/or $\frac{\partial h}{\partial t} > 0$. This is solved as a special case of AWIS with $B = 0, h = 0$. This is tested by first computing

$$\begin{aligned} \left(\frac{\partial B}{\partial t} \right)_0 &= \min \left(\frac{a_2}{a_4} - a_3 - \frac{m''_{in} c_w \tilde{\theta}_{rb,in}}{\rho_g L_F}, \frac{m''_{imp} + m''_{in} - m''_e}{\rho_r} \right) \\ \left(\frac{\partial h}{\partial t} \right)_0 &= \min \left(\frac{1}{\rho_w} \left\{ m''_{imp} + m''_{in} - m''_e - \rho_g \frac{\partial B}{\partial t} \right\}, \frac{m''_{imp} + m''_{in} - m''_e}{\rho_w} \right) \end{aligned} \quad (68)$$

If $\left(\frac{\partial B}{\partial t} \right)_0 > 0$ and $\left(\frac{\partial h}{\partial t} \right)_0 \leq 0$, then only rime ice will form ($\rho_i = \rho_r$). In this case,

$$\frac{\partial B}{\partial t} = \left(\frac{\partial B}{\partial t} \right)_0, \quad \frac{\partial h}{\partial t} = 0 \quad (69)$$

If $\left(\frac{\partial B}{\partial t}\right)_0 > 0$ and $\left(\frac{\partial h}{\partial t}\right)_0 > 0$, then both ice and water will form simultaneously, in which case,

$$\frac{\partial B}{\partial t} = \left(\frac{\partial B}{\partial t}\right)_0, \quad \frac{\partial h}{\partial t} = \left(\frac{\partial h}{\partial t}\right)_0 \quad (70)$$

If $\left(\frac{\partial B}{\partial t}\right)_0 < 0$ and $\left(\frac{\partial h}{\partial t}\right)_0 > 0$, then only water will form, in which case,

$$\frac{\partial B}{\partial t} = 0, \quad \frac{\partial h}{\partial t} = \frac{1}{\rho_w} \{m''_{imp} + m''_{in} - m''_e\}. \quad (71)$$

11. Air-Water-Substrate (AWS)

Boundary conditions:

$$-k_w \frac{\partial \theta}{\partial z} \Big|_{z=0} = H_{ws}(T_s - \theta(0, t)), \quad -k_w \frac{\partial \theta}{\partial z} \Big|_{z=h} = -Q_a - Q_k + Q_c + Q_d + Q_e. \quad (72)$$

Applying these boundary conditions, the temperature solution in the water layer is $\theta(z) = E_1 z + E_0$, where

$$E_0 = \frac{a_5(a_0 + a_1 T_a) + T_s(1 + a_1 h)}{1 + a_1(h + a_5)}, \quad E_1 = \frac{E_0 - T_s}{a_5}, \quad a_5 = \frac{k_w}{H_{ws}} \quad (73)$$

If the water temperature is above freezing, then ice will not form and $\frac{\partial B}{\partial t} = 0$ is set. However, if the water temperature reaches freezing, then the rate of ice formation is determined using Eq. 44 if $h < h^*$ (Case 1) or using Eq. 46 if $h \geq h^*$ (Case 2). If this yields $\frac{\partial B}{\partial t} < 0$, then $\frac{\partial B}{\partial t} = 0$ is set (since $B = 0$, it is not physically possible to have $\frac{\partial B}{\partial t} < 0$). The water film growth rate $\frac{\partial h}{\partial t}$ and exiting runback water mass flux m''_{out} are computed as described for the AWIS case.

12. Air-Ice-Substrate (AIS)

Boundary conditions:

$$-k_i \frac{\partial T}{\partial z} \Big|_{z=0} = H_{is}(T_s - T(0, t)), \quad -k_i \frac{\partial T}{\partial z} \Big|_{z=B} = -Q_a - Q_k - Q_\ell + Q_c + Q_d + Q_s. \quad (74)$$

Applying these boundary conditions, the temperature solution in the ice layer is $T(z) = D_1 z + D_0$, where

$$D_0 = \frac{a_4(a_0 + a_1 T_a) + T_s(1 + a_1 B)}{1 + a_1(B + a_4)}, \quad D_1 = \frac{D_0 - T_s}{a_4},$$

$$a_0 = \frac{r H_{ai} V_\infty^2}{2 c_a k_i} + \frac{\beta V_\infty^3 G}{2 k_i} + \frac{\rho_r L_f}{k_i} \left(\frac{\partial B}{\partial t}\right), \quad a_1 = \frac{H_{ai} + \beta V_\infty G c_w + \chi_s e_0}{k_i}, \quad a_4 = \frac{k_i}{H_{is}}, \quad (75)$$

To check whether only ice or both ice and water will form, Eq. 44 is first evaluated with $h = 0$ to obtain the rate of ice growth in the limiting case where water may begin to form.

$$\left(\frac{\partial B}{\partial t}\right)_0 = \frac{a_2}{a_4 + B} - \frac{a_3}{1 + a_1 h} - \frac{m''_{in} c_w \tilde{\theta}_{rb,in}}{\rho_g L_F}, \quad \left(m''_{frz}\right)_0 = \rho_g \left(\frac{\partial B}{\partial t}\right)_0 \quad (76)$$

If $\left(m''_{frz}\right)_0 \geq m''_{imp} + m''_{in} - m''_{evap}$, then no water will form. Only rime ice will form, and thus,

$$\frac{\partial B}{\partial t} = \frac{m''_{imp} + m''_{in} - m''_s}{\rho_r}, \quad \frac{\partial h}{\partial t} = 0. \quad (77)$$

On the other hand, if $\left(m''_{frz}\right)_0 < m''_{imp} + m''_{in} - m''_{evap}$, both ice and water will form. In this case,

$$\frac{\partial B}{\partial t} = \left(\frac{\partial B}{\partial t}\right)_0, \quad \frac{\partial h}{\partial t} = \frac{1}{\rho_w} \left(m''_{imp} + m''_{in} - m''_s - \rho_g \frac{\partial B}{\partial t}\right). \quad (78)$$

13. Air-Water-Ice-Water-Substrate (AWIWS)

Boundary conditions: For ice – $D_0 = T_f$, $D_1 = 0$; For water – Same as AWIS case

The ice/water interfaces are always assumed to be at the freezing temperature T_f . Therefore, there is no temperature gradient within the ice layer, which is at a uniform temperature T_f . The assumption for this case is that the layer of water beneath the ice is at a uniform temperature T_f . The heat transfer between the substrate at temperature T_s and the water (melted ice) above it is given by

$$Q_{surf} = H_{ws}(T_s - T_f). \quad (79)$$

The melting of ice results in a negative increment to the ice growth rate and the development of a water layer of thickness c beneath the ice layer. The growth rates are related to the surface heat flux Q_{surf} as

$$Q_{surf} = -\rho_g L_F \Delta \left(\frac{\partial B}{\partial t} \right), \quad \frac{\partial c}{\partial t} = \frac{\rho_g}{\rho_w} \Delta \left(\frac{\partial B}{\partial t} \right). \quad (80)$$

The ice growth rate for $h < h^*$ (Case 1) is now given by

$$\frac{\partial B}{\partial t} = -\frac{a_3}{1 + a_1 h} - \frac{m''_{in} c_w \tilde{\theta}_{rb,in}}{\rho_g L_F} - \frac{Q_{surf}}{\rho_g L_F}, \quad (81)$$

while that for $h \geq h^*$ (Case 2) is given by

$$\frac{\partial B}{\partial t} = \frac{1}{1 + c_w \tilde{\theta}_{rb,out} / L_F} \left\{ -\frac{a_3}{1 + a_1 h} - \frac{m''_{in} c_w \tilde{\theta}_{rb,in}}{\rho_g L_F} - \frac{Q_{surf}}{\rho_g L_F} + \frac{(m''_{imp} + m''_{in} - m''_e) c_w \tilde{\theta}_{rb,out}}{\rho_g L_F} \right\} \quad (82)$$

Finally, the water film growth rate $\frac{\partial h}{\partial t}$ and exiting runback water mass flux m''_{out} are computed in the same manner as for the AWIS case.

14. Air-Ice-Water-Substrate (AIWS)

Boundary conditions:

$$\begin{aligned} -k_i \frac{\partial T}{\partial z} \Big|_{z=B+c} &= (H_{ai} + \beta V_\infty G c_w + \chi_s e_0)(T(B+c, t) - T_a) - \frac{r H_{ai} V_\infty^2}{2 c_a} - \frac{\beta V_\infty^3 G}{2} - \rho_r L_f \left(\frac{\partial B}{\partial t} \right) \\ T(z=c, t) &= T_f \end{aligned} \quad (83)$$

With these boundary conditions, the temperature profile for ice is given by $T(z, t) = D_0 + D_1(z - c)$, where

$$\begin{aligned} D_0 &= T_f, \quad D_1 = \frac{a_0 - a_1(T_f - T_a)}{1 + a_1 B}, \\ a_0 &= \frac{r H_{ai} V_\infty^2}{2 c_a k_i} + \frac{\beta V_\infty^3 G}{2 k_i} + \frac{\rho_r L_f}{k_i} \left(\frac{\partial B}{\partial t} \right), \quad a_1 = \frac{H_{ai} + \beta V_\infty G c_w + \chi_s e_0}{k_i}. \end{aligned} \quad (84)$$

The incremental ice growth rate $\Delta \left(\frac{\partial B}{\partial t} \right)$ due to melting of ice from the bottom is computed using Equations 79-80. This is added to the basic ice growth rate calculated using Equations 76-78 to obtain the net growth rate of ice.

Appendix C: Classical Runge-Kutta

The classical Runge-Kutta method was set up in a vectorized fashion for integrating Eq. 11 to 15. For an initial value problem [23]

$$\dot{y} = f(t, y), \quad y(t_0) = y_0 \quad (85)$$

where y is the quantity to be integrated. The solution is given as,

$$y_{n+1} = y_n + (k_1 + 2k_2 + 2k_3 + k_4) \Delta t / 6 \quad (86)$$

$$t_{n+1} = t_n + \Delta t \quad (87)$$

for $n = 0, 1, 2, 3, \dots$ using

$$k_1 = f(t_n, y_n) \quad (88)$$

$$k_2 = f(t_n + \Delta t/2, y_n + \Delta t k_1/2) \quad (89)$$

$$k_3 = f(t_n + \Delta t/2, y_n + \Delta t k_2/2) \quad (90)$$

$$k_4 = f(t_n + \Delta t, y_n + \Delta t k_3) \quad (91)$$

By defining $\Delta t = \lambda \cdot \text{chord}/V_\infty$ (SI units) (with $\lambda \approx 0.002$) as constant for all droplets, a sufficiently small time step is ensured that maintains accuracy without increasing simulation time unreasonably. This also facilitates solving Eq. 11 to 15 for all particles simultaneously in a vectorized fashion inside MATLAB for a particular time step using Eq. 86 to 91. To verify the implementation of this classical Runge-Kutta integration scheme, the drag term defined by Eq. 14 can be set to zero. The droplets then undergo a pure projectile motion having been launched horizontally with initial velocity V_∞ , with only gravitational downward acceleration. The analytical and simulation results for this simplistic case match very closely.

Appendix D: Continuous Maximum Icing Conditions

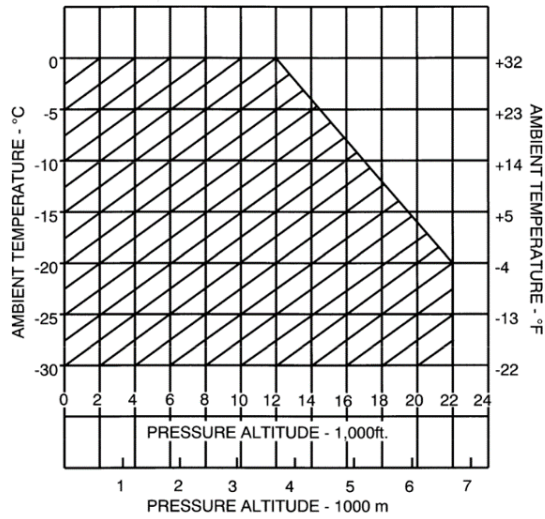


Fig. 15 Stratiform clouds ambient temperature vs. pressure altitude (FAR §25, Appendix C [6])

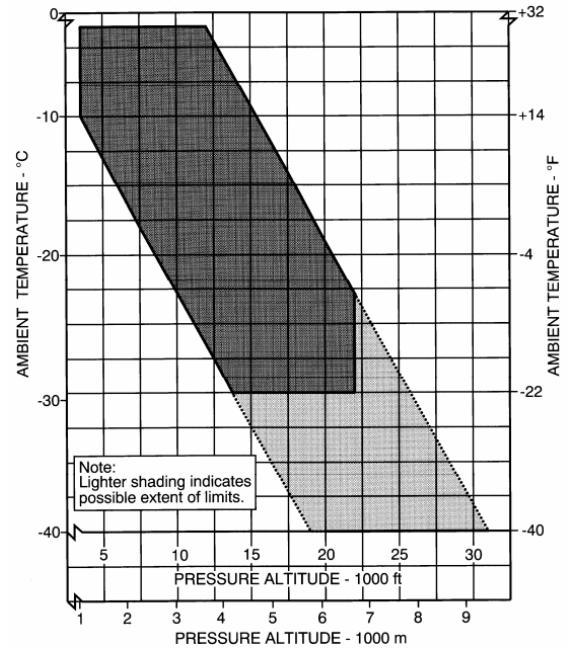


Fig. 16 Cumuliform clouds ambient temperature vs. pressure altitude (FAR §25, Appendix C [6])

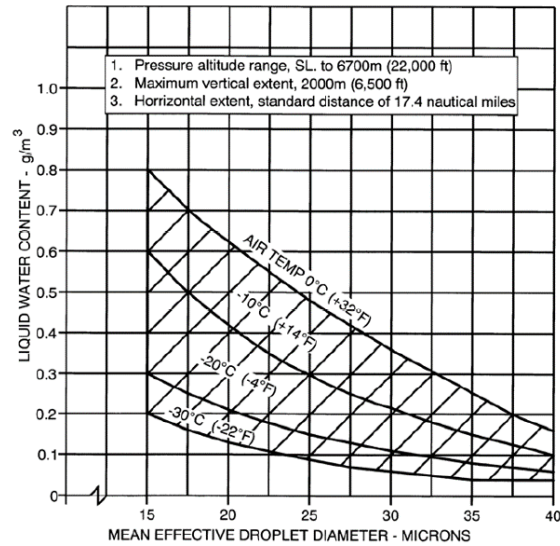


Fig. 17 Liquid Water Content vs. Mean Effective Droplet Diameter (FAR §25, Appendix C [6])

Acknowledgments

The authors would like to thank Fatma Karagoz, Ph.D student in Aerospace Engineering, Georgia Institute of Technology for her contributions to this research. The authors would also like to thank SAFRAN for funding foundational work leading to this paper.

References

- [1] Krammer, P., and Scholz, D., "Estimation of Electrical Power Required for Deicing Systems," Tech. rep., Hamburg University of Applied Sciences, July 2009.
- [2] Özgen, S., and Canibek, M., "Ice accretion simulation on multi-element airfoils using extended Messinger model," *Heat Mass Transfer*, Vol. 45, 2009, pp. 305–322.
- [3] Myers, T., and Hammond, D., "Ice and water film growth from incoming supercooled droplets," *International Journal of Heat and Mass Transfer*, Vol. 42, 1999, pp. 2233–2242.
- [4] Myers, T., "Extension to the Messinger Model for Aircraft Icing," *AIAA Journal*, Vol. 39, No. 2, 2001, pp. 211–218.
- [5] Heinrich, A., Ross, R., Zumwalt, G., Provorse, J., and Padmanabhan, V., "Aircraft Icing Handbook. Volume 1," Tech. rep., DTIC Document, 1991.
- [6] "Federal Aviation Regulations (FAR) Part 25 - Airworthiness Standards: Transport Category Airplanes," Federal Aviation Administration (FAA), 2018.
- [7] "Certification Specifications and Acceptable Means of Compliance for Large Aeroplanes: CS-25, Amendment 16," European Aviation Safety Agency (EASA), 2013.
- [8] "SAE Aerospace Applied Thermodynamics Manual - SAE AIR 1168," Society of Automotive Engineers (SAE), 1990.
- [9] Wright, W., "User's Manual for LEWICE Version 3.2," Tech. rep., NASA Glenn Research Center, 2008.
- [10] Shaw, R., Potapczuk, M., and Bidwell, C., "NASA's Program on Icing Research and Technology," Tech. Rep. NASA TM-101989, NASA Lewis Research Center, Cleveland, Ohio, May 1989.
- [11] Tran, P., Brahimi, M., Tezok, F., and Paraschivoiu, I., "Numerical simulation of ice accretion on multiple element configurations," *AIAA paper*, Vol. 869, 1996, p. 1996.
- [12] Thomas, S. K., Cassoni, R. P., MacArthur, C. D., et al., "Aircraft anti-icing and de-icing techniques and modeling," *Journal of Aircraft*, Vol. 33, No. 5, 1996, pp. 841–854.

- [13] Wauquiez, W., and Rizzi, A., “Potential Flow about Airfoils with Boundary Layer Coupled One-Way,” <http://www.pdas.com/pablo.html/>, 1999. [Online; accessed 11-June-2017].
- [14] Ketz, J., and Plotkin, A., *Low-speed aerodynamics: from wing theory to panel methods*, McGraw-Hill, Incorporated, 1991.
- [15] Anderson Jr, J. D., *Fundamentals of aerodynamics*, Tata McGraw-Hill Education, 2010.
- [16] “NACA 0012 Airfoil Validation Case,” NASA, online: https://turbmodels.larc.nasa.gov/naca0012_val.html, accessed November 8, 2017, 2017.
- [17] Sutherland, W., “LII. The viscosity of gases and molecular force,” *Philosophical Magazine Series 5*, Vol. 36, No. 223, 1893, pp. 507–531. doi:10.1080/14786449308620508, URL <http://dx.doi.org/10.1080/14786449308620508>.
- [18] Gent, R., Dart, N., and Cansdale, J., “Aircraft icing,” *Philosophical Transactions of the Royal Society of London A: Mathematical, Physical and Engineering Sciences*, Vol. 358, No. 1776, 2000, pp. 2873–2911.
- [19] Smith, A., and Spalding, D., “Heat Transfer in a Laminar Boundary Layer with Constant Fluid Properties and Constant Wall Temperature,” *Journal of the Royal Aeronautical Society*, Vol. 62, 1958, pp. 60–64.
- [20] Kays, W. M., and Crawford, M. E., *Convective Heat and Mass Transfer*, McGraw-Hill, 1980.
- [21] Myers, T., Charpin, J., and Thompson, C., “Slowly accreting ice due to supercooled water impacting on a cold surface,” *Physics of Fluids*, Vol. 14(1), 2002, pp. 240–256.
- [22] Chakraborty, I., and Mavris, D., “Integrated Assessment of Aircraft and Novel Subsystem Architectures in Early Design,” *Journal of Aircraft*, Vol. 54:4, 20017, pp. 1268–1282. doi:10.2514/1.C033976.
- [23] “The Runge Kutta Method,” https://en.wikipedia.org/wiki/Runge%E2%80%93Kutta_methods, 2017. [Online; accessed 26-June-2017].